Modelling active layer thickness in mountain permafrost based on an analytical solution of the heat transport equation, Kitzsteinhorn, Hohe Tauern Range, Austria.

Wolfgang Aumer[1,2], Ingo Hartmeyer[3], Carolyn-Monika Görres[1], Daniel Uteau[4], Stephan Peth[5]

[1]Geisenheim University, Department of Applied Ecology, Von-Lade-Straße 1, 65366 Geisenheim, Germany
[2]University of Kassel, Section of Ecological Plant Protection, Nordbahnhofstraße 1a, 37213 Witzenhausen, Germany
[3]GEORESEARCH Forschungsgesellschaft mbH, Wissenspark Salzburg-Urstein, Urstein Süd 13, 5412 Puch bei Hallein, Austria
[4]University of Kassel, Section of Soil Science, Nordbahnhofstraße 1a, 37213 Witzenhausen, Germany
[5]Leibniz University Hannover, Institute of Soil Science, Herrenhäuser Str. 2, 30419 Hannover, Germany

Correspondence to: Wolfgang Aumer (wolfgang.aumer@hs-gm.de)

Abstract. The active layer thickness (ALT) refers to the seasonal thaw depth of a permafrost body and is an essential parameter for natural hazard analysis, construction, land-use planning and the estimation of greenhouse gas emissions in periglacial regions. The aim of this study is to model the annual maximum thaw depth for determining ALT based on temperature data measured in four shallow boreholes (SBs, 0.1 m deep) in the summit region of the Kitzsteinhorn (Hohe Tauern Range, Austria, Europe). We set up our heat flow model with temperature data (2016-21) from a 30 m deep borehole (DB) drilled into bedrock at the Kitzsteinhorn north-face. For modeling purposes, we assume 1D conductive heat flow and present an analytical solution of the heat transport equation through sinusoidal temperature waves resulting from seasonal temperature oscillations (damping depth method). The model approach is considered successful: In the validation period (2019-21), modeled and measured ALT differed by only 0.1±0.1 m. We then applied the DB-calibrated model to four SBs and found that the modeled seasonal ALT maximum ranged between 2.5 m (SB 2) and 10.6 m (SB 1) in the observation period (2013-2021). Due to small differences in altitude (~ 200 m) within the study area, slope aspect had the strongest impact on ALT. To project future ALT deepening due to global warming, we integrated IPCC climate scenarios SSP1-2.6 and SSP5-8.5 into our model. By mid-century (~ 2050), ALT is expected to increase by 48 % at SB 2 and by 62 % at DB under scenario SSP1-2.6 (56 % and 128 % under scenario SSP5-8.5), while permafrost will no longer be present at SB 1, SB 3 and SB 4. By the end of the century (~ 2100), permafrost will only remain under scenario SSP1-2.6 with an ALT increase of 51 % at SB 2 and of 69 % at DB.

1 Introduction

Permafrost is defined as ground (soil or rock and the water contained therein) that remains frozen for at least two consecutive years (Harris et al., 1988) and is warming on a global scale (Biskaborn et al., 2019). In steep environments, such as the European Alps, warming-induced permafrost degradation is capable of destabilizing slopes and rock walls (Gruber et al., 2004;

Gude and Barsch, 2005; Fischer et al., 2006; Gruber and Haeberli, 2007; Krautblatter et al., 2013). Consequently, permafrost degradation is considered as one of the main causes for natural hazards in high-alpine areas and is expected to play a significant role in triggering a wide spectrum of mass movements ranging from debris flows (Stoffel et al., 2014), to medium-scale rockfalls (Legay et al., 2021) to large-scale rock avalanches such as recently witnessed at the Piz Cengalo (Walter et al., 2020)

35   or in 2023 at the Fluchthorn (Austria). In general, European mountain permafrost is characterized by ground temperatures just slightly below the freezing point (warm permafrost), and as a result is highly climate-sensitive (Harris et al., 2009). Direct ground temperature measurements have shown, in some parts very fast, warming in the European Alps within the last decades (Harris, 2003; Etzelmüller et al., 2020).

40   The active layer thickness (ALT) refers to the ground's thaw depth during the summer season. The seasonally thawed active layer is not permafrost by definition, but is a key parameter of permafrost bodies (Harris et al., 1988; Michaelides et al., 2019). In periglacial landscapes, geomorphological, ecological, hydrological and pedological processes take place almost exclusively within the active layer (Hinzman et al., 1991; Harris et al., 2009). ALT evolution over time thus represents a critical variable for hazard management and prevention, but also to accurately quantify greenhouse gas release from permafrost soils (Miner

45   et al., 2022). Microbial activity and the decay of organic matter is restricted to the active layer. Consequently, ALT data provide required information to investigate carbon-climate feedbacks in earth system models (Mishra et al., 2017). They are also required for land-use planning and construction on permafrost to warrant foundation stability and to avoid infrastructure damage (Hjort et al., 2022). In high-mountain regions exceptional rockfall activity has been observed as a direct response to the thickening or new formation of the active layer during hot summers, which potentially exposes deep-seated failure planes

50   to positive temperatures (e.g. Allen and Huggel, 2013; Ravanel et al., 2017). Due to its broad relevance across many disciplines, the Global Climate Observing System (GCOS, 2021) has recognized the ALT as an "Essential Climate Variable" (ECV), i.e., as a parameter that critically contributes to the characterization of Earth's climate (GCOS, 2021). ALT data are collected in a global database (GTN-P - Global Terrestrial Network for Permafrost) (Biskaborn et al., 2015), which reveals a worldwide trend towards ALT deepening (Biskaborn et al., 2019; Streletskiy et al., 2020; Kaverin et al., 2021).

55   Complex mountain topography (altitude, slope aspect, inclination) significantly modifies the amount of incoming solar radiation received by the ground surface. It thus has a pronounced effect on surface net energy input and leads to a high spatial variability of subsurface temperatures (Haeberli et al., 2010; Gubler et al., 2011). As a result, ALT varies strongly at the same elevation, ranging from few meters to more than ten meters (PERMOS, 2023). ALT can be precisely recorded through temperature measurements in deep boreholes. High-alpine drilling works are, however, technically challenging, expensive and

60   time-consuming, and only provide point recordings with limited spatial representation. The implementation of shallow boreholes (SBs) to record near-surface temperature (e.g. at 0.1 m depth), however, is simpler and allows significantly more measurement points (Hartmeyer et al., 2012), yet provides no direct ALT recordings due to an insufficient penetration depth. In this study, we used near-surface temperature data (0.1 m depth), which is widely available in permafrost regions, to simulate ALT based on the heat transport equation.

65 So far numerous studies of lowland (e.g. Burn and Zhang, 2009; Etzelmüller et al., 2011) and mountain permafrost (e.g. Engelhardt et al., 2010; Hipp et al., 2012) have simulated heat flow and ALT using 1D numerical models, which are well-suited to handle heterogenous material properties. For the first time, here we presented an analytical solution to the heat transport equation to model ALT in mountain permafrost at the borehole scale. Analytical solutions provide a direct mathematical description of the relationship between variables and therefore offer a concise, process-based understanding how

70 (modified) input parameters impact the studied system. This is of particular relevance in global-warming-related sensitivity analyses to estimate to which extent changes in input parameters (e.g. rising temperatures) impact the result of a model without the need for extensive simulations. Following De Vries (1963), we analytically solved the heat transport equation through sinusoidal thermal waves which propagate into the subsurface. A six-year dataset from a 30 m deep borehole (DB) at the Kitzsteinhorn (Austria) served as data base for model calibration and validation. The model was then used to simulate present-

75 day ALT at four SBs (0.1 m deep) located in the same study area, assuming identical thermal properties due to highly similar bedrock properties. In addition, we integrated IPCC (Intergovernmental Panel on Climate Change) climate projections (IPCC, 2023) into our model to simulate the ALT for mid and end of the century. The new approach was applied to a single mountain (Kitzsteinhorn summit pyramid), but is well-suited to model ALT on larger scales in complex high-mountain topography as well as in less complex (sub)polar lowland topography.

80 **2 Study Area**

The Kitzsteinhorn is part of the Hohe Tauern mountain range in the Central Eastern Alps (Austria). The highest point is at 3 203 m a.s.l. (47°11'17"N, 12°41'15"E). Because of the relative singularity of the mountain massif and a pyramidal summit structure, the study area is well suited to investigate the influence of slope aspect and elevation on ground temperatures. The climate at the Kitzsteinhorn, which is located just north of the main alpine ridge, is characterized by humid, high-alpine weather

85 conditions (Otto et al., 2012). In the vicinity of the study area (< 2 km), three weather stations are located at different altitudes. The stations at Glacier Plateau (GP) and Kammerscharte (KS) are closest to the boreholes investigated in this study, and annual air temperature of these two stations are very similar. Minimum temperatures occur in January and February, maximum temperatures in July and August. Table 1 summarizes the key information from the weather stations.

90 In the study area, permafrost distribution was simulated using the empirical-statistical model "PERMAKART 3.0", which estimates permafrost probability using a topo-climatic key for the Hohe Tauern mountain range (Schrott et al., 2012). Based on this simulation, permafrost can be expected with a very high probability (> 75 %) in an area of ~ 1.2 km² around the summit. Permafrost predominantly occurs on the northwest flank and, to a slightly lesser extent, on the northeast flank. In contrast, no significant occurrences of permafrost are to be expected on the south-exposed mountain flanks.

95

Most of the bedrock in the study area is made up of gray-blue (freshly fractured) and yellow-brown (with incipient weathering) calcareous mica schist (Krainer, 2005). Tectonic stress in combination with intense physical weathering has led to the formation of joints with large apertures (Hartmeyer et al., 2012). Optical borehole imaging carried out at the deep borehole (DB) immediately after drilling showed joint sizes apertures of a few mm up to several cm (usually < 5 cm) in first

100   couple of meters of the borehole. With increasing depth, the calcareous mica schist becomes more compact. Due to the schistosity, dipping steeply (~ 45°) towards north, the rock has an anisotropy for water and heat transport.

The study area hosts a long-term geoscientific monitoring project ("Open-Air-Lab Kitzsteinhorn") which was initiated in 2010 and investigates the impact of global warming on permafrost thaw and rock stability based on a combination of subsurface, surface and atmospheric measurements (Hartmeyer et al., 2012). The present study is based on the existing research

105   infrastructure and uses temperature data from a 30 m deep borehole (DB) and four shallow boreholes (SBs, 0.1 m deep), three of which are located in the immediate vicinity of the Kitzsteinhorn summit (Table 2, Fig. 1).

Table 1. Weather data from the three different stations Alpincenter (AC), Gletscherplateau (GP) and Kammerscharte (KS) in the vicinity of the study area (< 2 km), MAAT: mean annual air temperature.

Station	Altitude a.s.l (m)	MAAT (°C)	Slope of temperature over 10 a (°C)	Max. snow depth (m)	Mean global radiation (W m^{-2})
AC	2446	1.3	0.7	4.8	NA
GP	2920	(-2.3)	NA	(5.8)	(158)
KS	2561	-2.3	0.7	3.7	NA

110   **Data are daily mean values in the observation period from 01.01.2011 to 31.12.2021; data at the weather station GP for the years 2018, 2019 and 2020 are missing due to measurement failures (values in brackets); NA: not available.**

Table 2. Borehole locations and temperature logging depths in the study area.

Name	Altitude a.s.l (m)	Temperature sensor depths (m)	Slope aspect (°)	Inclination angle (°)
DB	2990	0.1, 1, 2, 3, 5, 7, 10, 15, 20, 25, 30	0 (N)	45
SB 1	2981	0.1	285 (WNW)	60
SB 2	3192	0.1	315 (NW)	40
SB 3	3196	0.1	65 (ONO)	80
SB 4	3198	0.1	160 (SO)	45

115   **Altitude a.s.l. refers to the entrance or the highest point of the boreholes. The boreholes were drilled perpendicular to the local inclination angle (DB: Deep borehole, SB: Shallow borehole).**

4
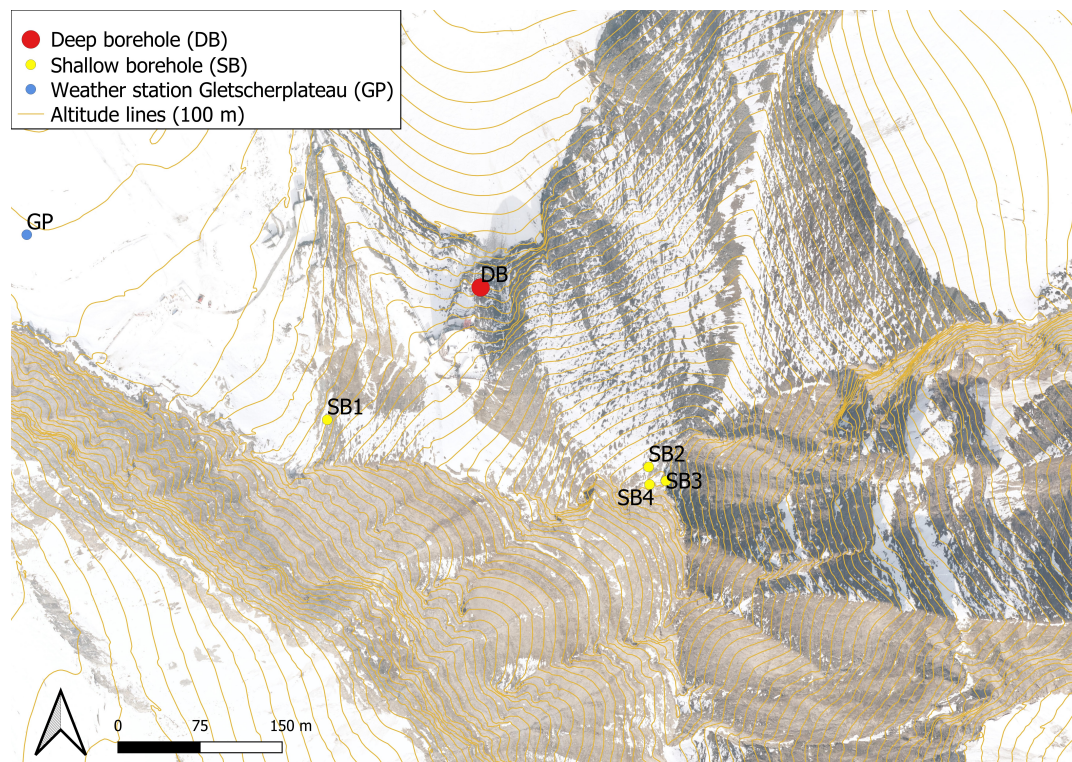
Figure 1: Borehole locations for temperature logging in the Kitzsteinhorn study area. The thermal model used to estimate active layer thickness (ALT) was calibrated and validated on the deep borehole (DB). Orthophoto and altitude lines: www.basemap.at.

3 Material and Methods

### 3.1 Temperature logging and data processing

The deep borehole (DB) was drilled with an air rotary drilling equipment (diameter 90 mm) to a depth of 30 m (Fig. 2a). The borehole was then instrumented with an innovative temperature measurement system consisting of a PVC-casing with brass segments at the designated sensor depths (Hartmeyer et al., 2012). Upon insertion of the thermistor chain, all temperature sensors establish direct contact with the casing's brass segments. Due to the high thermal conductivity of the brass segments (~ 110 W m^{-1} K^{-1}) this setup enables excellent thermal coupling between the temperature sensors and the surrounding bedrock (annulus was filled up with concrete). Temperature inside the DB is measured with Pt100 thermistors with an accuracy of ±0.03°C between -50 °C and 400 °C (Platinum Resistance Temperature Detector L220, 1/10 B, Heraeus Sensor Technology®, DE). In addition to the DB we used ground temperature data measured in four shallow boreholes (SBs, diameter 18 mm). The SBs were drilled to a depth of 0.1 m (Fig. 2b) and equipped with miniature temperature sensors. Prior to the installation, the sensors were glued to PVC rods (17 mm diameter) and then inserted into the SBs. After insertion, the borehole entrance was sealed watertight with silicone. The used sensors (Ibutton®, DS1922L, Maxim Integrated Products®, USA) consists of a button cell (steel housing) with an integrated computer chip, real-time clock and temperature sensor with an accuracy of

5

135 ±0.5 °C within the temperature range -10 to 65 °C. Extensive empirical testing with iButtons®, however, yielded an absolute
sensor accuracy of ±0.21 °C, underlining their suitability for high-quality thermal monitoring (Hubbart et al., 2005).

For model development (calibration and validation), DB daily mean temperature was used for the period 01 January 2016
to 31 December 2021. Daily mean values were determined based on twelve measurement points per day. Temperature data
were spline-interpolated (Δz = 10 cm) for better depth resolution between measurements. Due to polynomial adjustments of

140 the spline interpolation, positive interpolation values (< 0.1 °C) between two negative measurement values occurred in 39
cases. Since these interpolation values were not realistic they were set to 0 °C. The depth z (m) and time t (day) of the year
where temperature T(z,t) was above 0 °C were estimated from the measured and interpolated depth- and time-dependent
temperature data; daily thaw depths were derived subsequently. Model applications at the SBs were based on temperature
records in the period 01 January 2012 to 31 December 2021, however, large data gaps existed in some cases. Temperature in

145 the SBs was recorded every three hours and resulted in eight measurement points per day for daily mean temperature
calculations. (Note that in the whole study the mathematical sign plus minus (±) between two values stands for standard
deviation.)

(a)   **(b)**
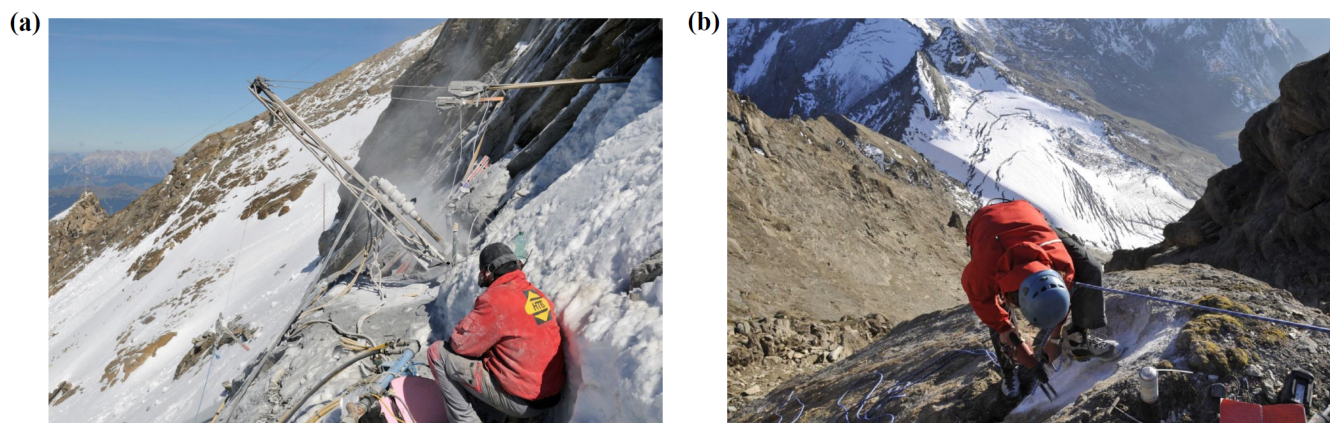
150 **Figure 2: (a) Drilling procedure (air-flushed rotary drilling) for a 30 m deep borehole (DB) on the western flank of the Kitzsteinhorn (Austria) (identical procedure to the DB used in this study). (b) Drilling of a shallow borehole (SB) for the installation of Ibuttons® for temperature logging at a depth of 0.1 m on the southern flank of the Kitzsteinhorn (2011). Due to the lower effort, more measuring points could be realized to address spatial variability. Photos by Ingo Hartmeyer.**

3.2 Thermal modelling

155 Conduction was assumed to be the only transport mechanism of heat flow, thus neglecting convection and latent heat release.
Conductive heat transport can be described by the heat transport equation, which describes temperature change as a function
of space and time (e.g. Williams and Smith, 1993):

$$\frac{\partial T}{\partial t} = \alpha \frac{\partial^2 T}{\partial z^2} \tag{1}$$

with $\partial T/\partial t$ being the first derivative with respect to time (Δt (s)), α is the thermal diffusivity ($m^2 s^{-1}$) and $\partial^2 T/\partial z^2$ is the second derivative in respect to position (Δz (m)) in terms of depth (z). The thermal diffusivity α ($m^2 s^{-1}$) is defined as the quotient of

160   the thermal conductivity λ ($J s^{-1} m^{-1} {}^\circ C^{-1}$) and the specific volumetric heat capacity C_V ($J m^{-3} {}^\circ C^{-1}$):

$$\alpha = \lambda / C_v \tag{2}$$

In our study, the heat transport equation was solved following an analytical approach: Under the assumption of a homogeneous ground, a harmonic sinusoidal temperature oscillation, and a mean ground temperature (T_m) that is constant with depth (z), the heat transport equation (Eq. 1) could be solved in one-dimension (z). The periodic temperature profile on the surface (z = 0) can be described as a function of time with the following sine function (DeVries 1963):

$$T_s = T_m + A_s \sin\left[\left(\frac{2\pi}{P}\right)(t - t_m)\right] \tag{3}$$

165   where T_s is the time dependent temperature at the surface (°C), T_m is the mean temperature at the surface in an annual or daily cycle, A_s is the temperature amplitude on the ground surface (°C), P is the period length (s), t is the time in the annual or daily cycle (s), and t_m (s) is the time in the period when $T_s = T_m$ (during the rise in temperature within a period). Given the set constraint of a constant mean ground temperature at each depth, a time-dependent temperature function for arbitrary depths could be established by using the sinusoidal function from Eq. 3:

$$T_{(t,z)} = T_m + A_s \exp^{\left(\frac{-z}{d}\right)} \sin\left[\left(\frac{2\pi}{P}\right)(t - t_m) - \frac{z}{d}\right] \tag{4}$$

170   Where $T_{(t,z)}$ is the temperature (°C) that depends on time (t, in seconds) and depth (z, in meters), d stands for the damping depth (m) and denotes the depth at which A_s has been damped to 37% while A_z denotes the damped amplitude at depth z. This extended temperature function can be used to simulate the amplitude damping and phase shift for any arbitrary depth. The damping depth is the fundamental parameter for the propagation of periodic temperature oscillations into depth and is related to the thermal diffusivity (α) over the period length P:

$$d = \sqrt{\left(\frac{\alpha P}{\pi}\right)} \tag{5}$$

175   Eq. 5 shows that besides the thermal diffusivity α, the period length is determining the damping depth. The expected damping depth in the annual cycle is greater than in the daily cycle by a factor of $365^{0.5} = 19.1$. If the damping depth is known, the thermal diffusivity can be calculated by converting Eq. 5 as follows:

$$\alpha = \frac{\pi}{P} \cdot d^2 \tag{6}$$

When using temperature measurements at two or more depths, the damping depth can be derived from the phase shift (d_{phase}) and the amplitude damping ($d_{amplitude}$). In the ideal case of a harmonic temperature oscillation, d_{phase} equals $d_{amplitude}$. Both can

180   be obtained graphically by using temperature measurements at two depths (z_1, z_2), defining minimum and maximum of the temperature wave and the time offset of the phases (t_1, t_2). By multiplying the slope by the factor $P/(2\pi)$, d_{phase} can be calculated,

7

$$d_{phase} = \frac{P}{2\pi} \cdot \frac{(z_1 - z_2)}{(t_1 - t_2)} \tag{7}$$

while for the calculation of $d_{amplitude}$, the depth (z_1, z_2) is plotted against the natural logarithm of the amplitudes (A_{z1}, A_{z2}), with the slope equal to the value of $d_{amplitude}$:

$$d_{amplitude} = \frac{(z_1 - z_2)}{\ln(A_{z1}) - \ln(A_{z2})} \tag{8}$$

As the annual thaw process and its maximum depth was the focus of this study, the high-frequency daily temperature
185   oscillations were neglected. A phase length of 365 days was assumed, resulting in a period length of 365 x 86400 s. Values for temperature at depth were calculated in a model via Eq. 4 with $\Delta z = 0.1$ m and $\Delta t = 24$ h. The chosen depth of 0.1 m, as a near-surface boundary condition, offers the advantage that temperature is undisturbed by turbulent heat flows on the ground surface. Furthermore, daily temperatures were smoothed with a moving average of five days. The year-specific mean temperatures in 0.1 m depth (T_m) were calculated using smoothed values. Therefore, the values of T_m differ minimally from
190   the calculated mean annual ground temperature (MAGT) in 0.1 m depth which was calculated without curve smoothing. Ground temperatures and the annual thaw process in the summer are influenced by the previous winter (Dobinski 2011). Therefore, the amplitudes were calculated based on half the difference in T_{min} and the T_{max} in the preceding summer months. Then t_m was determined as the day in each annual phase when $T_{(t,z)}$ first exceeded the value of T_m in the annual cycle. Since temperature oscillations at 0.1 m depth are very heterogeneous (even after smoothing), t_m was averaged from the six years
195   investigated.

   For model calibration (periods 2016 to 2018), the damping depth was adjusted ($d_{calibrated}$) to get the best match of the thawing process. For the model validation (periods 2019 to 2021), the values of daily thaw depths were tested using the Nash-Sutcliffe efficiency coefficient (NSE) (Nash and Sutcliffe 1970). The NSE is a quality criterion for model efficiency of time series, and it penalizes deviations more severely for high values than for small values. The values of the NSE can range from zero to one,
200   where one represents a perfect model fit. In accordance with Hipp et al. (2012), for successful modeling, we assume a threshold value of > 0.7. After the maximum of the annual thaw depth, the model showed large deviations from the measured values in each of the six years and could thus poorly represent the beginning freezing process. The modeled daily thaw depths were therefore only used to describe the thawing process and were modified on the day of maximum thaw depth by setting it to 0 m. The main emphasis of the model is not on the daily, but the annual max. thaw depths to determine ALT, for which the temporal
205   precision on a daily scale plays a minor role. The modeled values of annual thaw depths (validation period) were tested with the NSE and the root mean squared error (RMSE). The calculation of the damping depths from the phase shift over the annual temperature maxima (Eq. 7) and the amplitude damping (Eq. 8) helped to re-evaluate $d_{calibrated}$ to get a better interpretation of the model results.

   To be able to apply the model to the SBs, a basic assumption was that the damping depth is identical to the calibrated
210   damping depth ($d_{calibrated}$) determined at the DB, because the subsurface consisted of calcareous micaschist with highly similar properties at all locations. Climate projections were implemented by manipulating T_m following climate scenarios SSP1-2.6

and SSP5-8.5 (IPCC, 2023, Table SPM.1). When applying climate scenario SSP1-2.6, surface temperature is projected to increase by 1.6 °C and by 2.4 °C under SSP5-8.5 by mid-century (2041-2060), while by the end of the century (2081-2100), an increase of 1.8 °C is projected under scenario SSP1-2.6 and 4.4 °C under SSP5-8.5, respectively.

215 **4. Results**

4.1 Ground temperatures at the deep borehole

Temperature measurements at different profile depths are shown in Fig. 3a in the form of temperature oscillations of daily mean values. At 0.1 m depth, large overlaps of the annual temperature oscillations with the daily high-frequency temperature oscillations can be seen as pronounced noise. With increasing profile depth, the oscillations became more harmonic as short-
220 term atmospheric temperature fluctuations lost influence. Each year, there was a short period of time at the beginning of the frost period, when temperatures dropped below 0 °C, during which ground temperatures cooled slower and, in some cases, remained nearly constant for a short time period (zero-curtain effect). The zero-curtain effect was strongest at 3 m depth. At a depth of 30 m, the effect of the annual oscillations on the subsurface temperatures became almost negligible since the annual oscillation amplitudes had been almost completely dampened. During the study period (2016-2021), the annual mean
225 temperature minimum and maximum at this depth were -1.78±0.04 °C and -1.75±0.05 °C, respectively, and the seasonal temperature variations were less than 0.1 °C, indicating that the zero-annual amplitude (ZAA) was reached (Williams and Smith, 1993). Table 3 provides of characteristic values of the temperature wave at 0.1 m depth. The temperature data interpolated over depth (z) are shown in Fig. 3b.

230 **Table 3. Characteristic values of the annual temperature wave at 0.1 m depth at the north facing deep borehole (DB).**

| Year	T_{max}[1] (°C)	T_{min}[1] (°C)	Thaw index[1,2] (°Cd)	Frost index[1,2] (°Cd)	MAGT[1,3] (°C)	T_m[4] (°C)	A_s[5]
2016	9.54	-18.31	416	-1566	-3.14	-3.06	12.27
2017	9.99	-20.98	475	-1784	-3.55	-3.60	13.74
2018	9.04	-21.88	552	-1572	-2.79	-2.79	13.51
2019	13.08	-17.00	541	-1594	-2.88	-2.88	13.99
2020	8.46	-13.13	365	-1294	-2.57	-2.57	9.44
2021	10.75	-20.23	394	-1696	-3.58	-3.60	13.19
Mean	**10.14**	**-18.59**	**457**	**-1584**	**-3.09**	**-3.08**	**12.69**

[1]Values calculated without curve smoothing.

[2]The frost index is the temperature sum of all temperature values (daily averages) < 0 °C. Accordingly, the thaw index is the temperature sum of all temperature values (daily averages) > 0 °C.

[3]MAGT: mean annual ground temperature, calculated based on daily mean temperatures.

235 [4]T_m is the mean annual ground temperature used to drive the analytical model and calculated based on a five-day moving average of the daily mean temperature.

[5]A_s is the amplitude at 0.1 m depth used to drive the analytical model calculated from half the distance between the extreme values (T_{max} and T_{min}) of the annual temperature wave after curve smoothing (five-day moving average).
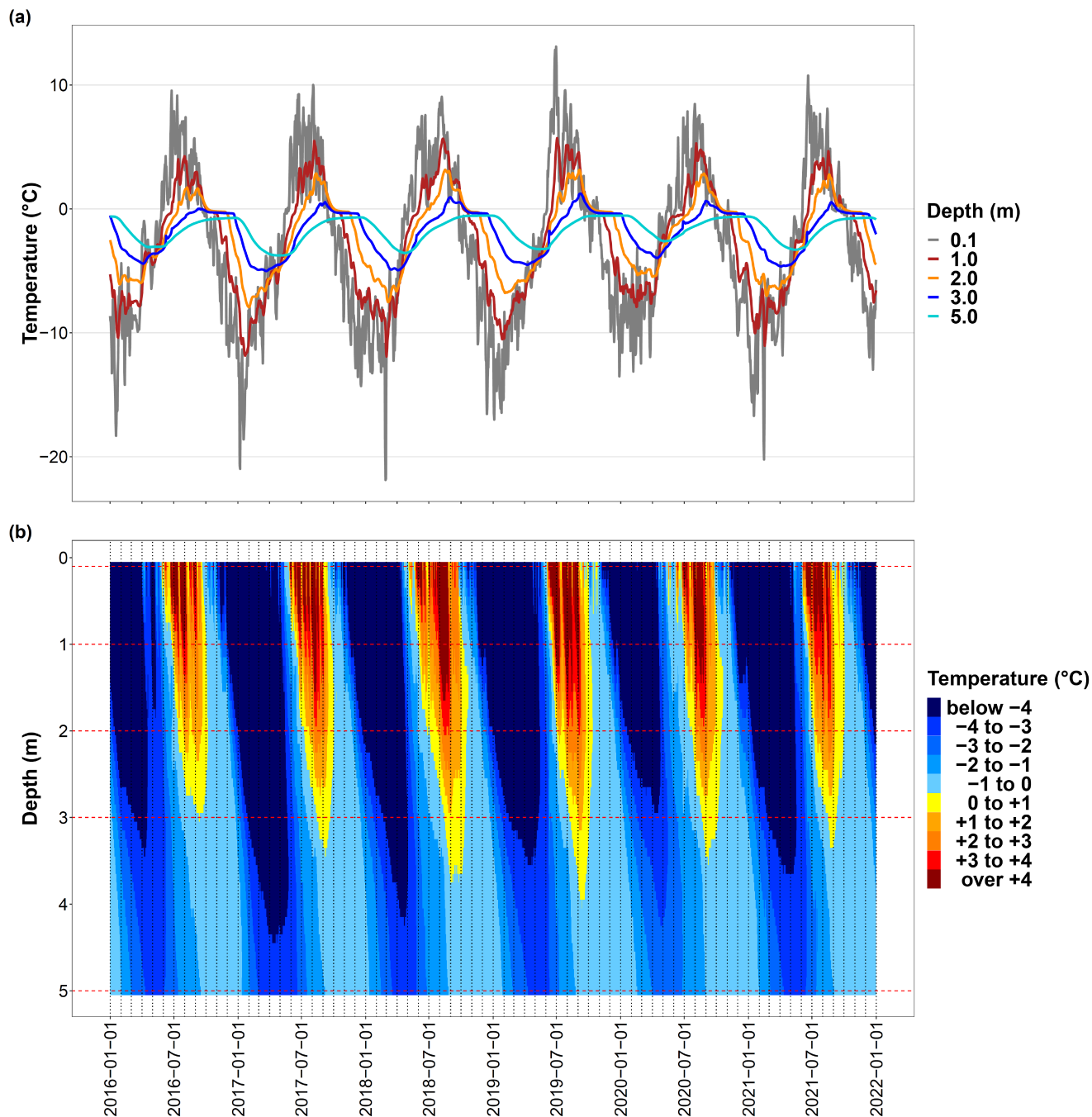
Figure 3: Temperature data and thawing process at the deep borehole (DB). (a) shows measured ground temperature (daily mean values) at different depths. (b) shows interpolated temperature data over depth and time (spline) as temperature classes. The red dashed cross lines refer to the depths at which temperature was measured (sensor depth).

Within the active layer, the mean annual ground temperature (MAGT) increased with depth (Fig. 4a). The mean thermal offset

245 was 1.23±0.23 °C between 0.1 m and 3 m depth (within the active layer) and 1.42±0.29 °C between 0.1 m to 5 m depth.

Accurate calculation of the damping depth from the phase shift (d_{phase}) was only possible for two years (2017 and 2018) and

across three measurement depths, due to inharmonic temperature oscillations in the other years. As shown in Fig. 4b, the phase

shift increased proportionally with depth, which is consistent with theory. In contrast, calculating the damping depth from the

amplitude damping ($d_{amplitude}$) was possible for all years. Down to a depth of 3 m, the amplitude damping was rather

250 homogeneous in depth (Fig. 4c). This indicates that thermal diffusivity was nearly constant down to that depth and that there

were no significant depth-dependent differences (e.g., due to water saturation changes). It also indicates that amplitudes were

exponentially more dampened with increasing depth, as expected from theory. Between 3 and 5 m depth, the amplitudes were

less dampened due to a higher thermal diffusivity. Here, the thermal diffusivity $\alpha_{amplitude}$ calculated from amplitude damping

was 0.89±0.22 x 10^{-6} m² s^{-1} on average over six years. For modeling the annual thaw process and ALT, the thermal diffusivity

255 between 0.1 and 3 m (within the active layer) is more important.
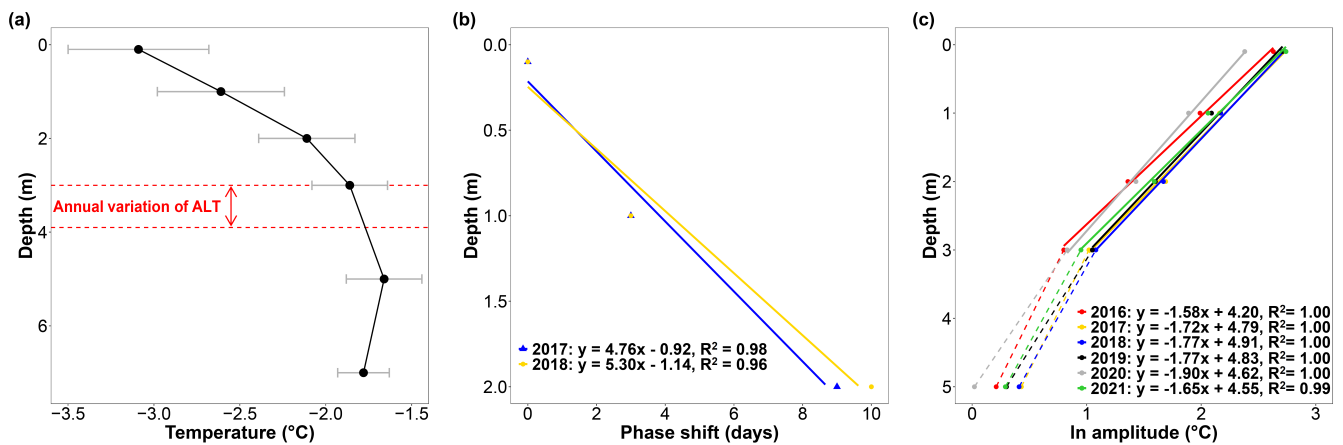
Figure 4: (a) mean values of the mean annual ground temperature (MAGT) at different depths from 2016 to 2021. Due to measurement failures, the data from 2020 and 2021 are missing at a depth of 7 m. The error bars show the standard deviation of the
260 **interannual variations. (b) phase shift of the annual temperature wave with depth and the corresponding regression lines. (c) Damping of the annual temperature amplitude with depth and the corresponding regression lines. Amplitude damping to a depth of 3 m was very homogeneous (R^2 close to 1). The scattered lines show the amplitude damping between 3 m and 5 m depth (not included for calculating regression lines), i.e. within the permafrost. The amplitude damping between active layer and permafrost was lower than in the profile above.**

265

Table 4 summarizes the estimated damping depths and calculated thermal diffusivities of the active layer, where the values of

d_{phase} were larger than those of $d_{amplitude}$. Two basic theoretical assumptions for the analytical solution of the heat equation

(Eq. 4) warranted a critical assessment, which is why the thermal diffusivities calculated via Eq. 6 (Table 4) could only be

regarded as approximations: First, the MAGT was only constant to a rough approximation due to the thermal offset with depth.

270 Second, the investigated temperature waves do not describe harmonic oscillations. This could already be seen in Fig. 3a and

11

was further confirmed by the fact that d_{phase} was 0.97 m larger than $d_{amplitude}$. The damping depth calibrated via the modeling process ($d_{calibrated}$) was 2.4 m and thus lay within the interval of d_{phase} and $d_{amplitude}$ and relatively close to the mean value of d_{phase} and $d_{amplitude}$, which was 2.2 m.

275 **Table 4. Damping depths from phase shift (d_{phase}) and amplitude damping ($d_{amplitude}$) and the corresponding calculated thermal diffusivities (α_{phase}, $\alpha_{amplitude}$).**

Year	d_{phase} (m)	$d_{amplitude}$(m)	α_{phase} x 10^{-6} (m² s⁻¹)	$\alpha_{amplitude}$ x 10^{-6} (m² s⁻¹)
2016	(1.99)	1.58	(0.40)	0.25
2017	2.86	1.72	0.81	0.29
2018	2.54	1.77	0.64	0.31
2019	(4.65)	1.77	(2.15)	0.31
2020	(2.79)	1.90	(0.77)	0.36
2021	(6.97)	1.65	(4.84)	0.27
Mean	**2.70**	**1.73**	**0.73**	**0.30**

The values of d_{phase} without brackets were calculated between 0.1 and 2 m depth using linear regression over three depths (0.1, 1, 2 m). In contrast, the values of d_{phase} in brackets were only calculated over two depths (1-2 m) without linear regression and were not included in the mean value calculation due to high uncertainty. The values of $d_{amplitude}$ were calculated using linear regression
280 **over four depths (0.1, 1, 2, 3 m). To calculate the thermal diffusivity α, a period length (P) of 365 days was assumed.**

4.2 Modelling active layer thickness at the deep borehole

The daily thaw depths could be modeled satisfactory (NSE > 0.7) (Fig. 5a and 5b). The main modeling focus were the annual max. thaw depth for determining active layer thickness (ALT). In 2016 (calibration period), the model showed the largest
285 deviation from the measured value (Fig. 5a). In that year, the surface penetrating amplitude was also damped the most (Fig. 4c) and $\alpha_{amplitude}$ was consequently the smallest (Table 4). For the remaining years, annual max. thaw depths could be modeled with satisfactory accuracy over the entire study period. In the validation period (three data pairs), the RMSE was 0.13, the NSE was 0.76, which was well above the required threshold of 0.7 and the modeled ALT was very close to measured ALT (Fig. 5c).
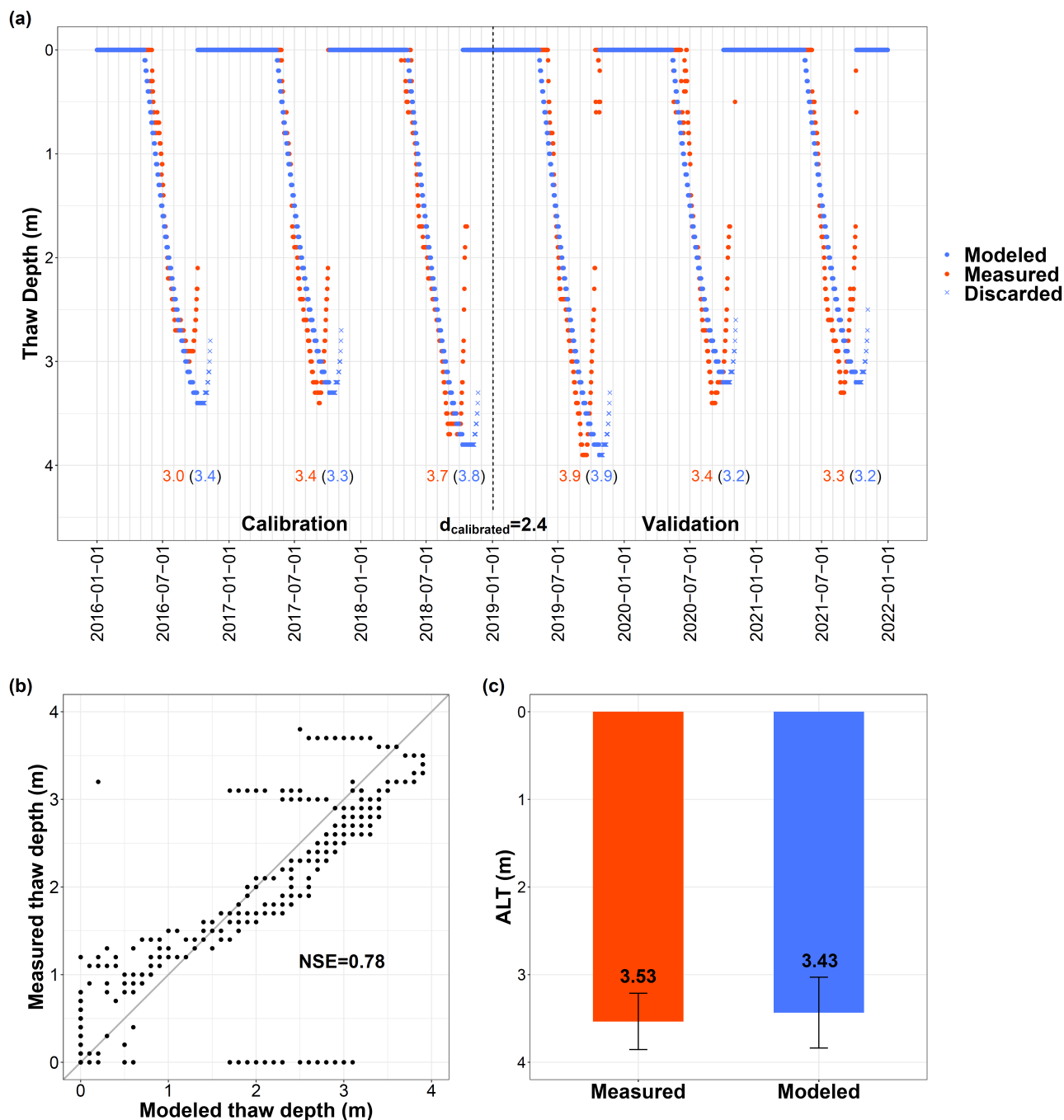
Figure 5: (a) Daily measured and modeled thaw depths at the deep borehole (DB). The given numbers represent the annual maximum thaw depth. The calibrated damping depth ($d_{calibrated}$) expresses the thermal diffusivity for thermal wave propagation with depth. The autumnal frost process could not be represented well, so modeled values for the time after the annual thaw depth maximum were discarded and replaced by the value zero. **(b)** Scatterplot of daily measured and modeled thaw depths for the validation period; gray line = line of equality; NSE=Nash-Sutcliffe efficiency coefficient. **(c)** Mean values of the measured and modeled active layer thickness (ALT) of the validation period; the error bars show the standard deviation.

13

4.3 Spatial and future projection of active layer thickness

Table 5 shows ALT values for the studied deep borehole (DB) and the four shallow boreholes (SBs). The west- (SB 1), east- (SB 3), and south-facing (SB 4) boreholes (Table 2) were the warmest (Appendix B). At SB 3, five out of seven modelled
300 years showed a positive MAGT calculated with a sliding average for analytical modelling (T_m, see section 3.2); no two consecutive years with a negative T_m were found. This indicates that permafrost was not present there. Permafrost was present at SB 1 and SB 4, but one year with a positive T_m was also observed at each of the two sites. In contrast to SB 1 and SB 4, which had similarly high ALT values, the two north-facing boreholes (DB and SB 2) showed a much smaller ALT. In direct comparison, the ALT at SB 2 was 0.5±0.2 smaller than at DB (average of 2016 to 2019).

305

Table 5. Measured (deep borehole = DB) and modeled (shallow borehole = SB) values of the annual maximum thaw depths in m.

Year	DB	SB 1	SB 2	SB 3	SB 4
2013	-	6.3	2.7	-	7.2
2014	-	5.1	-	NP	5.1
2015	-	6.9	-	10.4	9.4
2016	3.0	8.1	2.5	NP	-
2017	3.4	6.8	3.1	6.8	-
2018	3.7	10.6	3.3	NP	10.3
2019	3.9	NP	3.1	NP	NP
2020	3.4	8.2	-	NP	8.4
2021	3.3	6.8	-	-	5.8

NP = no permafrost, (-) indicates data gaps due to measurement failures.

Following SSP1-2.6, permafrost will no longer be present at SB 1, SB 3, and SB 4 by mid-century after an increase in T_m.
310 Projections of the future ALT could only be made for the coldest north-exposed boreholes DB and SB 2 (Fig. 6). Towards mid-century, the model showed an increase in the ALT of 48 % under SSP1-2.6 and 76 % under SSP5-8.5. Towards the end of the century, permafrost at SB 2 can only be expected under scenario SSP1-2.6 with an ALT increase of 51 %. At the slightly warmer DB, the model showed a 62 % increase in the ALT under SSP1-2.6 and a 128 % increase under SSP5-8.5 toward mid-century. Toward the end of the century, permafrost at DB can only be expected under scenario SSP1-2.6 with a 69 % increase
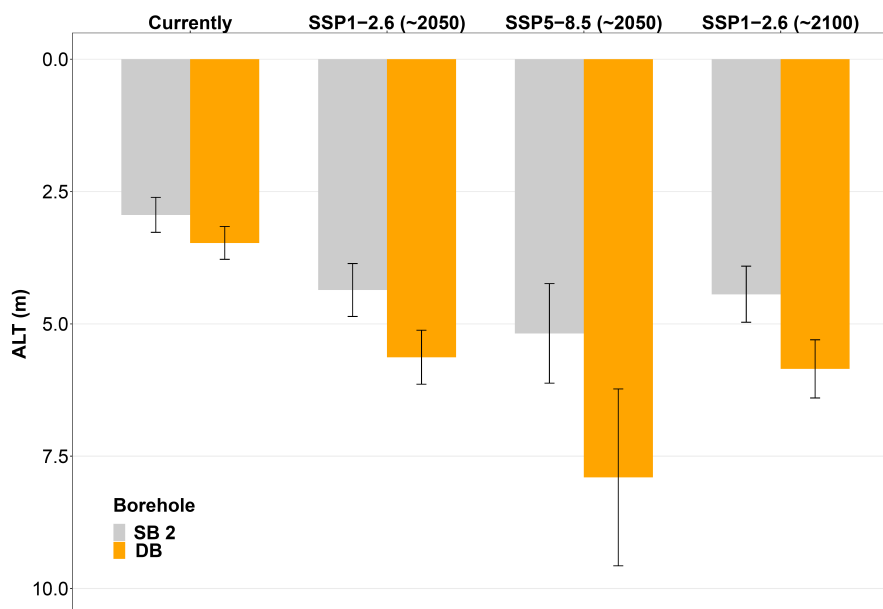315 in the ALT.

Figure 6: Projections of future ALT assuming scenarios SSP1-2.6 and SSP5-8.5 at the mid and end of the century at the deep borehole (DB) and shallow borehole 2 (SB 2). Towards the end of the century, permafrost can only be expected to occur in these two coldest, north-facing boreholes under scenario SSP1-2.6. The current ALT was calculated on the basis of all measured values during the study period, whereby the years included in the calculation were different in some cases (see Table 5). The colored bars show the mean values, the error bars the standard deviation.

5. Discussion

5.1 Ground temperatures at the deep borehole

The mean annual ground temperature (MAGT) rises with increasing depth within the active layer. This positive thermal offset of the MAGT with depth is surprising. An opposite (negative) thermal offset is a well-known phenomenon in polar regions (Burn and Smith, 1988; Romanovsky and Osterkamp, 1995; Smith and Riseborough, 2002) and was also already detected in mountain (bedrock) permafrost (Hasler et al., 2011), usually caused by a seasonal variation of the water saturation and its phase changes in the subsurface (Gruber and Haeberli, 2007). These variations cause the cooling front to usually penetrate the profile more deeply than the heating front resulting in a negative thermal offset. However, Hasler et al. (2011) also observed a positive thermal offset within the active layer for one out of nine temperature observations in mountain (bedrock) permafrost.

At the deep borehole (DB), the positive thermal offset was likely caused by (i) advective heat flow due to significant subsurface meltwater flow during the thaw period, combined with (ii) an increase in thermal diffusivity due to increased water saturation with depth: During the onset of the thaw season (~June), we observed sudden, sharp temperature jumps at 3 m depth, which can only be explained by fluid heat flow (convection) in fractures (and not by conduction-driven warming). This observation is consistent with optical scan data from the deep borehole (DB), which demonstrates open, surface-parallel (~ 45°) joints along the natural schistosity of the bedrock (calcareous mica-schist) that form ideal pathways for subsurface lateral water

15

flow. In addition, the zero-curtain effect observed in the measured temperature waves, which is caused by release and consumption of latent heat during the phase change of water/ice (Outcalt et al., 1990), became more pronounced with increasing depth and was especially strong at 3 m depth. At the end of the thaw period, water saturation at depth was therefore
340   increased.

Depth-dependent damping of annual amplitudes was very homogeneous, and consequently, no large changes are to be expected for vertical heat transport over the depth range studied. However, this refers to the damping of annual amplitudes and therefore does not necessarily exclude temporary water flow - which likely is responsible for the observed thermal offset. Within the permafrost body, i.e., below the active layer, amplitude damping was less pronounced. This is most likely related
345   to the phase change of fissure water, since ice has a thermal diffusivity roughly five (James, 1968) to eight times (Oke, 1987; Garratt, 1994) higher than liquid water.

5.2 Modelling active layer thickness at the deep borehole

We successfully modeled the ALT with an analytical solution of the heat transport equation based on near-surface temperature data (0.1 m depth). The accuracy of the modeled ALT was satisfactory, modeled and measured values of ALT differed by only
350   0.1±0.1 m during the validation period, with a Nash-Sutcliffe efficiency coefficient (NSE) value of 0.76, which was well above the threshold of 0.7 required for successful modeling (see section 3.2). The largest deviation between measured and modeled ALT was observed for 2016 (calibration period), with a value of 0.4 m. In that year, the surface penetrating temperature amplitudes were damped the most, and the calculated thermal diffusivity ($\alpha_{amplitude}$) was the smallest during the study period. In line with that, the largest differences between the calibrated damping depth ($d_{calibrated}$) and the damping depth calculated
355   from amplitude damping ($d_{amplitude}$) were also observed in 2016. No significant structural changes are expected in the bedrock of the calcareous mica-schist over the study period. Therefore, it is reasonable that a lower water content decreased thermal conductivity (Kim and Oh, 2019) and thus $\alpha_{amplitude}$, and as a result caused the largest model deviations in that year.

For the application of the analytical solution of the heat transport equation, two basic assumptions have to be considered critically: First, the MAGT was not constant at depth (z) or was constant only as a very rough approximation. Second, the annual
360   temperature waves did not describe harmonic oscillations. Temporal variability of weather conditions is the main reason for the deviation of annual air and ground temperature oscillations from an ideal sinusoidal pattern (Rajeev and Kodikara, 2016). Nevertheless, the good calibration and validation possibilities at DB permitted a relatively robust estimation of the damping depth ($d_{calibrated}$) for the vertical heat transport. In ideal harmonic oscillations, the values of d_{phase} and $d_{amplitude}$ are approximately equal. This was not the case in our study, however, the calibrated damping depth $d_{calibrated}$ (2.2 m) was in the interval of d_{phase} and
365    $d_{amplitude}$ and relatively close to the mean value of d_{phase} and $d_{amplitude}$ (2.4 m). This indicates a high plausibility that $d_{calibrated}$ can physically describe the vertical conductive heat transport for modeling the thawing process. Via an analytical solution of the heat transport equation, the local thermoregime can be representatively captured. The idealized forcing of the model provides the basis for performing relatively simple scenario-based future projections based on the manipulation of the surface temperature as boundary condition.

5.3 Spatial and future projection

Following model development with data from the DB, we applied the model to the shallow boreholes (SBs) and integrated IPCC climate scenarios for future ALT simulations. Due to the study area's uniform lithology, we assumed that thermal properties at the SBs did not significantly differ in thermal properties at the DB, and that $d_{calibrated}$ can be transferred to the SBs. Minor spatial variations of the thermal properties may still introduce uncertainty into the model application at the SBs, however, our modeling approach offers the advantage that the spatial variability of the local thermal regime is excluded and the actual influence of topographic factors can be better captured. Thus, ALT can be estimated on a larger spatial scale, and subsequently, conclusions can be drawn about rock and slope stability.

In the study area, slope aspect is the dominant topographic factor influencing ALT due to low elevation differences between the investigated boreholes (~ 200 vertical meters). As a result, the smallest ALT (2.5-3.9 m) was found at the two north-facing boreholes DB and SB 2, which are both characterized by clear permafrost conditions. Large ALT values between five and ten meters were found at SB 1 and SB 4. Under current climatic conditions no permafrost is indicated for SB 3, the subsurface, however, could still contain relict permafrost produced by cooler conditions in the past. Somewhat surprisingly, apart from 2019, the south-facing borehole SB 4 is slightly colder (T_m, Table B1) and thus has a higher permafrost probability than the east-facing borehole SB 3. This is most likely related to differences in rockwall gradients and their impact on the local snow cover. The south-facing borehole SB 4 is located in a moderately steep rockwall section that hosts a thick snowpack during winter, spring and early summer. While this insulation efficiently prevents the propagation of cold winter temperatures into the subsurface (warming effect), it also leads to a significant delay of seasonal warming (cooling effect) as compared to the east-facing SB 3, which is exposed to direct sunlight the entire year and, due to its steep gradient (~ 80°), absorbs significant amounts of solar radiation even at low sun angles (winter season).

ALT projection under scenario SSP5-8.5 suggests that, by mid-century, mountain permafrost will only be present at the north-facing boreholes and that ALT will increase considerably. Toward the end of the century, permafrost will no longer be encountered also at these two coldest boreholes under this scenario. A conclusion transferable from this projection to other permafrost regions is that a larger initial ALT (DB: 2.9 compared to SB 2: 3.5) will also result in a larger increase in ALT for the same temperature increase (regarding to SSP5-8.5 for mid-century, SB 2: 56%, DB: 128%). This shows that in warm permafrost, even small changes in temperature cause large changes in ALT, which has significant implications for rock and slope stability. Study results from the Western Alps point to increased rockfall activity along the lower permafrost boundary, i.e. in regions with (already) large ALT. Rockfall documentations from Switzerland demonstrate a late-summer peak in rockfall activity in regions with warm permafrost around 3000 m a.s.l. (Kenner and Phillips, 2017) and analyses of a century-long inventory of slope failures from the central European Alps (France, Italy, Switzerland) indicate increased mass wasting in low-lying permafrost regions (Fischer et al., 2012). As climate warming is expected to continue or even accelerate, this trend will most likely be reinforced over the next decades. Warming-induced upward migration of the lower permafrost boundary may

result in a slight altitudinal shift of rockfall activity, while active layer thickening will most likely activate deeper failure planes and cause larger rockfall volumes – and will require significantly deeper foundations for constructions on permafrost.

6. Conclusions

405   The active layer thickness (ALT) of a permafrost body and its evolution over time is highly sensitive to climatic changes and of direct relevance in many important fields such as natural hazard analysis, construction, land-use planning and greenhouse gas emission studies. In the present study, we used borehole temperature data from the summit region of the Kitzsteinhorn (Central Eastern Alps, Austria) to model the annual maximum thaw depths for ALT analyses. We draw the following conclusions:

410   •   To model ALT, we analytically solved the heat transport equation through sinusoidal thermal waves which propagate into the subsurface. A six-year dataset from a 30 m deep bedrock borehole was used for model calibration and validation. So far simulations of the ALT were based on numerical models, the present study reports the first analytical solution to the heat transport equation to model ALT in mountain permafrost (borehole scale) and offers a concise, process-based understanding how (modified) input parameters impact the studied system.

415   •   Measured and modeled ALT values were highly consistent: During the validation period (2019-21), modeled and measured ALT at the deep borehole (DB) differed by only 0.1±0.1 m. The Nash-Sutcliffe efficiency coefficient (NSE) equaled 0.76 and therefore was well above the threshold of 0.7 required for successful modeling.

   •   We used the developed thermal model to simulate ALT at four shallow boreholes (SBs, 0.1 m deep), in the immediate vicinity and found that the modeled seasonal maximum of the ALT ranged between 2.5 m (SB 2) and 10.6 m (SB 1) in

420   the observation period (2013-2021). Due to small differences in altitude ($\sim$ 200 m) within the study area, slope aspect had the strongest impact on the ALT.

   •   Under the more moderate SSP1-2.6 scenario by mid-century, ALT is expected to increase by 48 % at SB 2 and by 62 % at DB, while permafrost will no longer exist at SB 1, SB 3 and SB 4.

   •   The effect of an increase in temperature on ALT is enhanced by a higher initial ALT. This indicates that in warm

425   permafrost even small changes in temperature cause large changes in ALT, which has significant implications for rock and slope stability.

   •   The introduced analytical solution of the heat transport equation was here applied to a single mountain, but in general is well-suited to simulate ALT on larger scales in complex high-mountain topography as well as less complex (sub)polar lowland topography.

430 **Appendix A: Measured and interpolated temperature data at the deep borehole.**
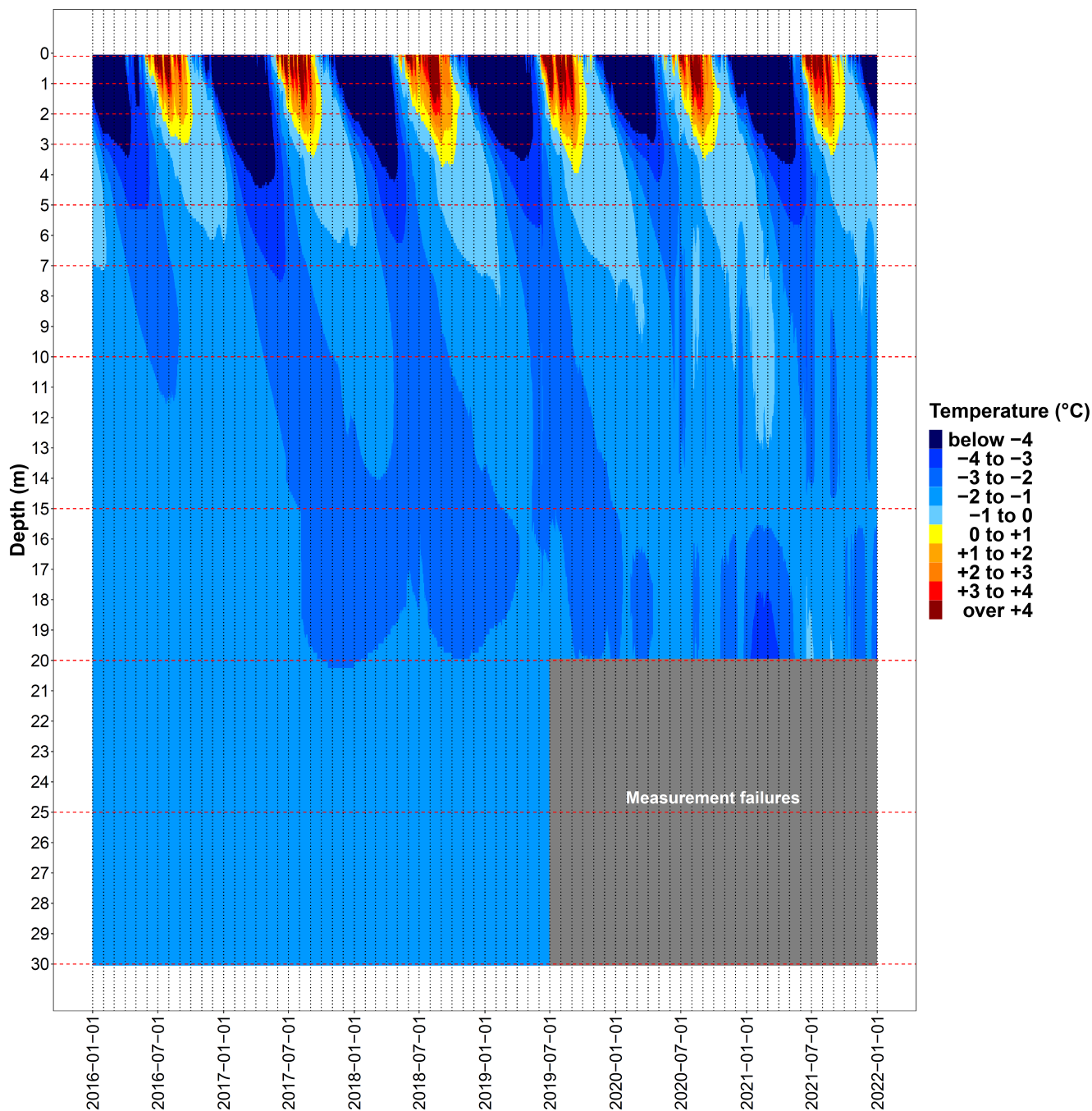
Figure A1: Interpolated temperature data over depth and time (spline) as temperature classes. The red dashed cross lines refer to the depths at which temperature was measured (sensor depth). In the gray filled area, the values could not be displayed accurately due to measurement gaps. The temperature sensor at 7 m depth has also failed since 14.06.2020, which is why the interpolation 435 values between 5 and 10 m may be less precise from then on.

19

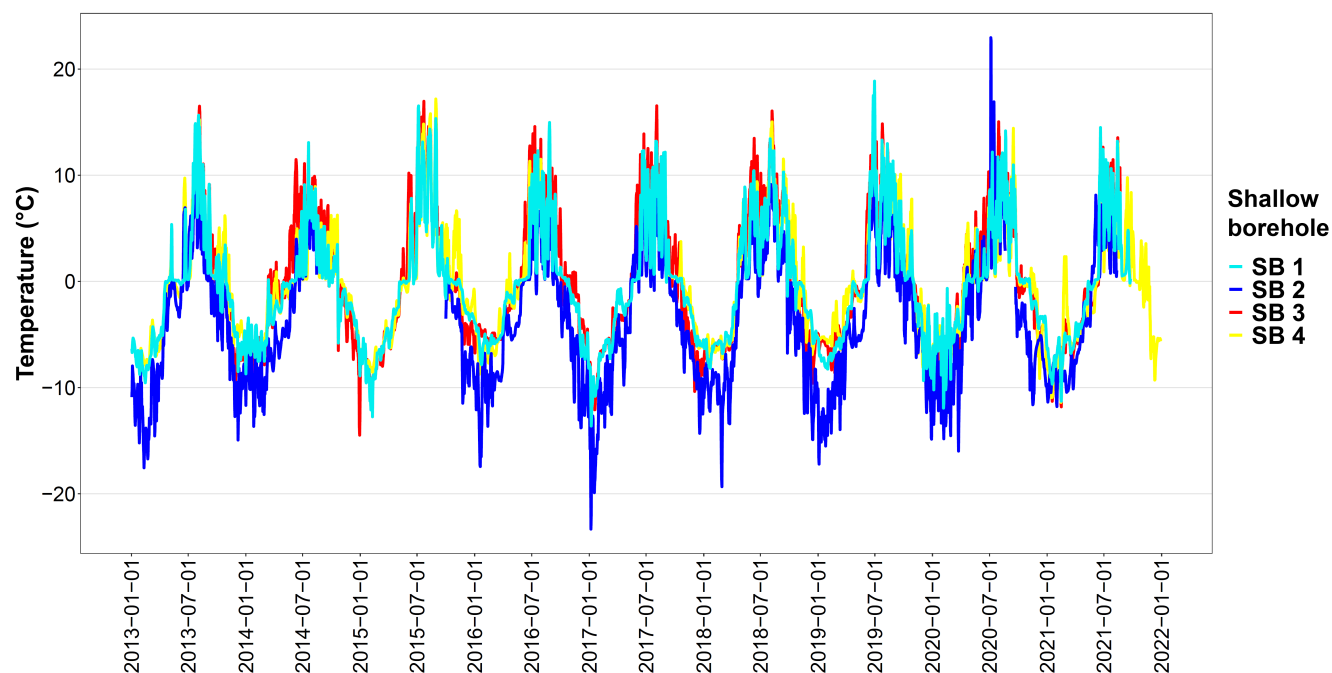**Appendix B: Temperature data at the four shallow boreholes.**

Figure B1: Measured ground temperature (daily mean values) at the investigated shallow boreholes (SBs). In some cases, there were large gaps in the data, in which case the temperature lines are shown as interrupted.

440

Table B1. Values for the analytical modeling, calculated from the temperature wave at a depth of 0.1 m in °C.

Year	SB 1		SB 2		SB 3		SB 4	
	T_m	A_s	T_m	A_s	T_m	A_s	T_m	A_s
2013	-0.88	11.91	-4.24	12.50			-0.58	11.32
2014	-1.02	8.24	-	-	0.01	11.18	-0.90	7.42
2015	-0.73	12.73	-	-	-0.18	13.37	-0.25	11.99
2016	-0.36	10.43	-4,10	11.40	0.33	9.64	-	-
2017	-0.77	12.56	-3,99	14.38	-0.79	13.13	-	-
2018	-0.12	10.10	-3,33	12.65	0.56	11.47	-0.16	11.02
2019	0.13	12.57	-3,63	12.77	0.09	13.06	0.64	11.12
2020	-0.34	10.22	-	-	0.22	11.48	-0.28	9.00
2021	-0.66	11.12	-	-	-	-	-1.04	-1.04

The temperature wave (daily averaged temperatures) was smoothed with a moving average of five days. T_m is the mean annual ground temperature and A_s is the temperature amplitude calculated from half the distance between the extreme values (T_{max} and T_{min}) of the annual temperature wave. Both model parameters served as surface boundary conditions for analytical modeling.

Data availability

The data that support the findings of this study are openly available in the repository Zenodo at https://doi.org/10.5281/zenodo.10203390 (Aumer and Hartmeyer, 2023).

445 **Competing interests**

We have no competing interests to declare.

Author contributions

WA took the lead in writing the manuscript with support from IH, CMG, DU and SP. IH provided the temperature data while WA derived the models and analysed the data. All authors contributed to the manuscript revision and approved the final
450 version.

455 **References**

Allen, S. and Huggel, C.: Extremely warm temperatures as a potential cause of recent high mountain rockfall, Global and Planetary Change, 107, 59–69, https://doi.org/10.1016/j.gloplacha.2013.04.007, 2013.

Aumer, W. and Hartmeyer, I.: Borehole temperatures and thaw depths in mountain permafrost, Kitzsteinhom, Hohe Tauern Range, Austria [Data set], Zenodo, https://doi.org/10.5281/zenodo.10203390, 2023.

460 Biskaborn, B. K., Lanckman, J.-P., Lantuit, H., Elger, K., Streletskiy, D. A., Cable, W. L., and Romanovsky, V. E.: The new database of the Global Terrestrial Network for Permafrost (GTN-P), Earth Syst. Sci. Data, 7, 245–259, https://doi.org/10.5194/essd-7-245-2015, 2015.

Biskaborn, B. K., Smith, S. L., Noetzli, J., Matthes, H., Vieira, G., Streletskiy, D. A., Schoeneich, P., Romanovsky, V. E., Lewkowicz, A. G., Abramov, A., Allard, M., Boike, J., Cable, W. L., Christiansen, H. H., Delaloye, R., Diekmann, B.,
465 Drozdov, D., Etzelmüller, B., Grosse, G., Guglielmin, M., Ingeman-Nielsen, T., Isaksen, K., Ishikawa, M., Johansson, M., Johannsson, H., Joo, A., Kaverin, D., Kholodov, A., Konstantinov, P., Kröger, T., Lambiel, C., Lanckman, J.-P., Luo, D., Malkova, G., Meiklejohn, I., Moskalenko, N., Oliva, M., Phillips, M., Ramos, M., Sannel, A. B. K., Sergeev,

D., Seybold, C., Skryabin, P., Vasiliev, A., Wu, Q., Yoshikawa, K., Zheleznyak, M., and Lantuit, H.: Permafrost is warming at a global scale, Nature communications, 10, 264, https://doi.org/10.1038/s41467-018-08240-4, 2019.

470   Burn, C. R. and Zhang, Y.: Permafrost and climate change at Herschel Island (Qikiqtaruq), Yukon Territory, Canada, J. Geophys. Res., 114, F02001, https://doi.org/10.1029/2008JF001087, 2009.

Burn, C. R. and Smith, C.: Observations of the "Thermal Offset" in Near-Surface Mean Annual Ground Temperatures at Several Sites near Mayo, Yukon Territory, Canada, ARCTIC, 41, 99–104, https://doi.org/10.14430/arctic1700, 1988.

Engelhardt, M., Hauck, C., and Salzmann, N.: Influence of atmospheric forcing parameters on modelled mountain
475   permafrost evolution, metz, 19, 491–500, https://doi.org/10.1127/0941-2948/2010/0476, 2010.

Etzelmüller, B., Guglielmin, M., Hauck, C., Hilbich, C., Hoelzle, M., Isaksen, K., Noetzli, J., Oliva, M., and Ramos, M.: Twenty years of European mountain permafrost dynamics—the PACE legacy, Environ. Res. Lett., 15, 104070, https://doi.org/10.1088/1748-9326/abae9d, 2020.

Etzelmüller, B., Schuler, T. V., Isaksen, K., Christiansen, H. H., Farbrot, H., and Benestad, R.: Modeling the temperature
480   evolution of Svalbard permafrost during the 20th and 21st century, The Cryosphere, 5, 67–79, https://doi.org/10.5194/tc-5-67-2011, 2011.

Fischer, L., Purves, R. S., Huggel, C., Noetzli, J., and Haeberli, W.: On the influence of topographic, geological and cryospheric factors on rock avalanches and rockfalls in high-mountain areas, Nat. Hazards Earth Syst. Sci., 12, 241–254, https://doi.org/10.5194/nhess-12-241-2012, 2012.

485   Fischer, L., Kääb, A., Huggel, C., and Noetzli, J.: Geology, glacier retreat and permafrost degradation as controlling factors of slope instabilities in a high-mountain rock wall: The Monte Rosa east face, Nat. Hazards Earth Syst. Sci., 6, 761–772, https://doi.org/10.5194/nhess-6-761-2006, 2006.

Garratt, J.: Review: the atmospheric boundary layer, Earth-Science Reviews, 37, 89–134, https://doi.org/10.1016/0012-8252(94)90026-4, 1994.

490   GCOS: The Status of the Global Climate Observing System 2021: The GCOS Status Report (GCOS-240), World Meteorological Organization, Geneva, Italy, 2021.

Gruber, S. and Haeberli, W.: Permafrost in steep bedrock slopes and its temperature-related destabilization following climate change, J. Geophys. Res., 112, https://doi.org/10.1029/2006JF000547, 2007.

Gruber, S., Hoelzle, M., and Haeberli, W.: Permafrost thaw and destabilization of Alpine rock walls in the hot summer of
495   2003, Geophys. Res. Lett., 31, n/a-n/a, https://doi.org/10.1029/2004GL020051, 2004.

Gubler, S., Fiddes, J., Keller, M., and Gruber, S.: Scale-dependent measurement and analysis of ground surface temperature variability in alpine terrain, The Cryosphere, 5, 431–443, https://doi.org/10.5194/tc-5-431-2011, 2011.

Gude, M. and Barsch, D.: Assessment of geomorphic hazards in connection with permafrost occurrence in the Zugspitze area (Bavarian Alps, Germany), Geomorphology, 66, 85–93, https://doi.org/10.1016/j.geomorph.2004.03.013, 2005.

500 Haeberli, W., Noetzli, J., Arenson, L., Delaloye, R., Gärtner-Roer, I., Gruber, S., Isaksen, K., Kneisel, C., Krautblatter, M., and Phillips, M.: Mountain permafrost: development and challenges of a young research field, J. Glaciol., 56, 1043–1058, https://doi.org/10.3189/002214311796406121, 2010.

Harris, C.: Warming permafrost in European mountains, Global and Planetary Change, 39, 215–225, https://doi.org/10.1016/j.gloplacha.2003.04.001, 2003.

505 Harris, C., Arenson, L. U., Christiansen, H. H., Etzelmüller, B., Frauenfelder, R., Gruber, S., Haeberli, W., Hauck, C., Hölzle, M., Humlum, O., Isaksen, K., Kääb, A., Kern-Lütschg, M. A., Lehning, M., Matsuoka, N., Murton, J. B., Nötzli, J., Phillips, M., Ross, N., Seppälä, M., Springman, S. M., and Vonder Mühll, D.: Permafrost and climate in Europe: Monitoring and modelling thermal, geomorphological and geotechnical responses, Earth-Science Reviews, 92, 117–171, https://doi.org/10.1016/j.earscirev.2008.12.002, 2009.

510 Harris, S. A., French, H. M., Heginbottom, J. A., Johnston, G. H., Ladanyi, B., Sego, D. C., and van Everdingen, R. O.: Glossary of permafrost and related ground-ice terms, National Research Council of Canada. Associate Committee on Geotechnical Research. Permafrost Subcommittee, ISBN0-660-12540-4, https://doi.org/10.4224/20386561, 1988.

Hartmeyer, Keuschnig M, and Schrott L: Long-term monitoring of permafrost-affected rock faces – A scale-oriented approach for the investigation of ground thermal conditions in alpine terrain, Kitzsteinhorn, Austria, Austrian Journal of
515 Earth Sciences, 105, 128–139, 2012.

Hasler, A., Gruber, S., and Haeberli, W.: Temperature variability and offset in steep alpine rock and ice faces, The Cryosphere, 5, 977–988, https://doi.org/10.5194/tc-5-977-2011, 2011.

Hinzman, L. D., Kane, D. L., Gieck, R. E., and Everett, K. R.: Hydrologic and thermal properties of the active layer in the Alaskan Arctic, Cold Regions Science and Technology, 19, 95–110, https://doi.org/10.1016/0165-232X(91)90001-W,
520 1991.

Hipp, T., Etzelmüller, B., Farbrot, H., Schuler, T. V., and Westermann, S.: Modelling borehole temperatures in Southern Norway – insights into permafrost dynamics during the 20th and 21st century, The Cryosphere, 6, 553–571, https://doi.org/10.5194/tc-6-553-2012, 2012.

Hjort, J., Streletskiy, D., Doré, G., Wu, Q., Bjella, K., and Luoto, M.: Impacts of permafrost degradation on infrastructure,
525 Nat Rev Earth Environ, 3, 24–38, https://doi.org/10.1038/s43017-021-00247-8, 2022.

Hubbart, J., Link, T., Campbell, C., and Cobos, D.: Evaluation of a low-cost temperature measurement system for environmental applications, Hydrol. Process., 19, 1517–1523, https://doi.org/10.1002/hyp.5861, 2005.

IPCC: Summary for Policymakers, in: Masson-Delmotte, V., P. Zhai, A. Pirani, S.L. Connors, C. Péan, S. Berger, N. Caud, Y. Chen, L. Goldfarb, M.I. Gomis, M. Huang, K. Leitzell, E. Lonnoy, J.B.R. Matthews, T.K. Maycock, T. Waterfield,
530 O. Yelekçi, R. Yu, and B. Zhou (eds.).: Climate Change 2021: The Physical Science Basis, Contribution of Working Group I to the Sixth Assessment Report of the Intergovernmental Panel on Climate Change, Cambridge University Press, Cambridge, United Kingdom and New York, NY, USA, 3–32, https://doi.org/10.1017/9781009157896.001, 2023.

James, D. W.: The thermal diffusivity of ice and water between -40 and +60 °C, J Mater Sci, 3, 540–543, https://doi.org/10.1007/BF00549738, 1968.

535 Kaverin, D., Malkova, G., Zamolodchikov, D., Shiklomanov, N., Pastukhov, A., Novakovskiy, A., Sadurtdinov, M., Skvortsov, A., Tsarev, A., Pochikalov, A., Malitsky, S., and Kraev, G.: Long-term active layer monitoring at CALM sites in the Russian European North, Polar Geography, 44, 203–216, https://doi.org/10.1080/1088937X.2021.1981476, 2021.

Kenner, R. and Phillips, M.: Fels- und Bergstürze in Permafrost Gebieten: Einflussfaktoren, Auslösemechanismen und
540 Schlussfolgerungen für die Praxis: Schlussbericht Arge Alp Projekt ‚Einfluss von Permafrost auf Berg- und Felsstürze', WSL-Institute For Snow And Avalanche Research SLF, Graubünden, 2017.

Kim, D. and Oh, S.: Relationship between the thermal properties and degree of saturation of cementitious grouts used in vertical borehole heat exchangers, Energy and Buildings, 201, 1–9, https://doi.org/10.1016/j.enbuild.2019.07.017, 2019.

Krainer, K.: Nationalpark Hohe Tauern: Geologie, 2., überarb. und erw. Aufl., Wissenschaftliche Schriften / Nationalpark
545 Hohe Tauern, Universitätsverlag Carinthia, Klagenfurt, 199 pp., ISBN3853785859, 2005.

Krautblatter, M., Funk, D., and Günzel, F. K.: Why permafrost rocks become unstable: a rock-ice-mechanical model in time and space, Earth Surf. Process. Landforms, 38, 876–887, https://doi.org/10.1002/esp.3374, 2013.

Legay, A., Magnin, F., and Ravanel, L.: Rock temperature prior to failure: Analysis of 209 rockfall events in the Mont Blanc massif (Western European Alps), Permafrost and Periglacial Processes, 32, 520–536, https://doi.org/10.1002/ppp.2110,
550 2021.

Michaelides, R. J., Schaefer, K., Zebker, H. A., Parsekian, A., Liu, L., Chen, J., Natali, S., Ludwig, S., and Schaefer, S. R.: Inference of the impact of wildfire on permafrost and active layer thickness in a discontinuous permafrost region using the remotely sensed active layer thickness (ReSALT) algorithm, Environ. Res. Lett., 14, 35007, https://doi.org/10.1088/1748-9326/aaf932, 2019.

555 Miner, K. R., Turetsky, M. R., Malina, E., Bartsch, A., Tamminen, J., McGuire, A. D., Fix, A., Sweeney, C., Elder, C. D., and Miller, C. E.: Permafrost carbon emissions in a changing Arctic, Nat Rev Earth Environ, 3, 55–67, https://doi.org/10.1038/s43017-021-00230-3, 2022.

Oke, T. R.: Boundary layer climates, Second edition, Routledge, London, New York, 435 pp., ISBN9780203407219, https://doi.org/10.4324/9780203407219, 1987.

560 Otto, J., Keuschnig, M., Götz, J., Marbach, M., and Schrott, L.: Detection of mountain permafrost by combining high resolution surface and subsurface information – an example from the glatzbach catchment, austrian alps, Geografiska Annaler: Series A, Physical Geography, 94, 43–57, https://doi.org/10.1111/j.1468-0459.2012.00455.x, 2012.

Outcalt, S. I., Nelson, F. E., and Hinkel, K. M.: The zero-curtain effect: Heat and mass transfer across an isothermal region in freezing soil, Water Resour. Res., 26, 1509–1516, https://doi.org/10.1029/WR026i007p01509, 1990.

565 PERMOS: Swiss Permafrost Bulletin 2022, Swiss Permafrost Monitoring Network, Noetzli, J. and Pellet, C. (eds.), No. 4, 22 pp., https://doi.org/10.13093/PERMOS-BULL-2023, 2023.

Ravanel, L., Magnin, F., and Deline, P.: Impacts of the 2003 and 2015 summer heatwaves on permafrost-affected rock-walls in the Mont Blanc massif, The Science of the total environment, 609, 132–143, https://doi.org/10.1016/j.scitotenv.2017.07.055, 2017.

570 Romanovsky, V. E. and Osterkamp, T. E.: Interannual variations of the thermal regime of the active layer and near-surface permafrost in northern Alaska, Permafrost and Periglacial Processes, 6, 313–335, https://doi.org/10.1002/ppp.3430060404, 1995.

Schrott, Jan-Christoph Otto, and Felix Keller: Modelling alpine permafrost distribution in the Hohe Tauern region, Austria, Austrian Journal of Earth Sciences, 169–183, 2012.

575 Smith, M. W. and Riseborough, D. W.: Climate and the limits of permafrost: a zonal analysis, Permafrost and Periglacial Processes, 13, 1–15, https://doi.org/10.1002/ppp.410, 2002.

Stoffel, M., Mendlik, T., Schneuwly-Bollschweiler, M., and Gobiet, A.: Possible impacts of climate change on debris-flow activity in the Swiss Alps, Climatic Change, 122, 141–155, https://doi.org/10.1007/s10584-013-0993-z, 2014.

Streletskiy, D. A., Shiklomanov, N. I., Nelson, F. E., Klene, A. E., Nyland, K. E., and Moore, N. J.: Global Observation Data
580 Show Variable but Increasing Active-Layer Thickness, American Geophysical Union, Fall Meeting, abstract #C016-07, 2020.

Walter, F., Amann, F., Kos, A., Kenner, R., Phillips, M., Preux, A. de, Huss, M., Tognacca, C., Clinton, J., Diehl, T., and Bonanomi, Y.: Direct observations of a three million cubic meter rock-slope collapse with almost immediate initiation of ensuing debris flows, Geomorphology, 351, 106933, https://doi.org/10.1016/j.geomorph.2019.106933, 2020.

585 Williams and Smith: The frozen earth. Fundamentals of geocryology., Permafrost and Periglacial Processes, 4, 178–181, https://doi.org/10.1002/ppp.3430040221, 1993.